How Friendly are Building Materials as Reflectors to Indoor LOS MIMO Communications?

Yixin Zhang, *Student Member, IEEE*, Chen Chen, *Student Member, IEEE*, Songjiang Yang, *Student Member, IEEE*, Jiliang Zhang, *Senior Member, IEEE*, Xiaoli Chu, *Senior Member, IEEE*, Jie Zhang, *Senior Member, IEEE*

***Abstract*—The tremendous popularity of internet of things (IoT) applications and wireless devices have prompted a massive increase of indoor wireless traffic. To further explore the potential of indoor IoT wireless networks, creating constructive interactions between indoor wireless transmissions and the built environments becomes necessary. The electromagnetic (EM) wave propagation indoors would be affected by the EM and physical properties of the building material, e.g., its relative permittivity and thickness. In this paper, we construct a new multipath channel model by characterising wall reflection (WR) for an indoor line-of-sight (LOS) single-user multiple-input multiple-output (MIMO) system and derive its ergodic capacity in closed-form. Based on the analytical results, we define the wireless friendliness of a building material based on the spatially averaged indoor capacity and propose a scheme for evaluating the wireless friendliness of building materials. Monte Carlo simulations validate our analytical results and manifest the significant impact of the relative permittivity and thickness of a building material on indoor capacity, indicating that the wireless friendliness of building materials should be considered in the planning and optimisation of indoor wireless networks. The outcomes of this paper would enable appropriate selection of wall materials during building design, thus enhancing the capacity of indoor LOS MIMO communications.**

***Index Terms*—Building material, wireless friendliness, indoor communications, EM wave, reflection, LOS, MIMO.**

I. Introduction

Internet of things (IoT) connects numerous heterogeneous devices, and provides infrastructures for smart buildings [1], [2], smart grids [3], and smart cities [4]. With the roll-out of 5G systems and the opening horizon of 6G systems, cellular networks will provide economical, flexible and reliable wireless connectivities for IoT devices, e.g., by leveraging 5G massive machine type communication (mMTC) [5] and 6G massive broad bandwidth machine type (mBBMT) [6] technologies.

It is predicted that 80-96% of wireless data traffic will be consumed indoors in the future [7]. As a result, indoor wireless traffic required by IoT is growing at an unprecedented rate. Notably, physical obstacles like walls would affect the indoor propagation of electromagnetic (EM) waves. Therefore, indoor wireless performance should be one of the indispensable prerequisites when designing buildings [8], [9].

To meet the high data demand and address the capacity crunch in-building, indoor small base stations (BSs) are usually equipped with large-scale antenna arrays [10], e.g. consisting of hundreds of antennas, facilitated by multiple-input multiple-output (MIMO) technology to achieve spatial multiplexing/diversity gains [11]–[13]. In order to guarantee a low spatial correlation, the space intervals among antenna elements of the MIMO antenna array have to be larger than half wavelength [14], which therefore will increase the physical dimension of the indoor small BSs and generate negative weight and visual consequence on a room. Especially in industrial environment, deploying BSs in the workspace may increase the risk of accidents.

To avoid any possible negative impact on the functionality and appearance of a room, a desirable indoor BS deployment is to integrate MIMO antenna arrays with interior walls [15], [16], which however will result in non-negligible coupling between MIMO antenna arrays and building materials [17]–[19]. Specifically, when an EM wave impinges on a wall surface, the intensity of the wall reflected wave can be measured by the reflection coefficient, which depends on the EM and physical properties of the wall material, i.e., its relative permittivity and thickness [20]–[25]. The wall reflected EM waves would be superposed with other EM waves, which may jointly influence the indoor wireless performance. Hence, enhancing indoor wireless performance requires a rational selection and/or design of building materials. In this paper, we define the wireless friendliness as a new performance metric of a building material, which is characterised by its relative permittivity and thickness. A building material with desirable wireless friendliness would be beneficial to the performance of indoor wireless networks.

Metamaterials are known as novel artificial structures, which can be customized to build a programmable EM propagation environment [26]. The meta-atoms in metamaterials are software-controlled to firstly capture the signals from the source and then reflect the signal to the destination actively or passively [27], [28]. Although metamaterials are expected to contribute to indoor capacity improvement, they are facing major challenges such as their design complexity growing exponentially with the number of meta-atoms. Besides, the energy efficiency of metamaterial-aided wireless networking is no better than massive MIMO [29] and relay-supported transmissions [30].

By contrast, the wireless friendliness of concrete as a widely

Yixin Zhang, Chen Chen, Songjiang Yang, Jiliang Zhang, and Xiaoli Chu are with the Department of Electronic and Electrical Engineering, University of Sheffield, S10 2TN, UK. E-mail: jiliang.zhang@sheffield.ac.uk.

Jie Zhang is with the Department of Electronic and Electrical Engineering, University of Sheffield, Sheffield, S10 2TN, UK, and also with Ranplan Wireless Network Design Ltd., Cambridge, CB23 3UY, UK.

This work was supported in part by the European Union's Horizon 2020 Research and Innovation Programme under Grant 766231 and Grant 752644.

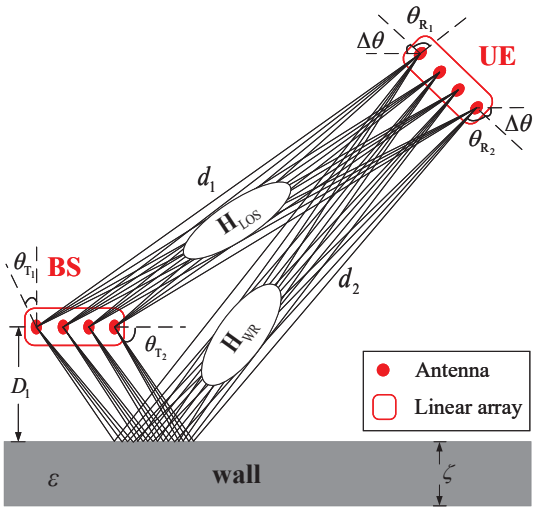

Fig. 1. The LOS path and the WR path between indoor BS and UE.

used building material has not been sufficiently studied. Most of the existing works on the EM wave propagation loss through concrete walls were based on measurements [31]–[33]. As far as we know, a theoretical analysis of indoor multipath capacity influenced by the EM and physical properties of concrete is still missing. As will be shown in the subsequent sections, the appropriate selection of building materials will increase the baseline value of indoor capacity. Accordingly, the wireless performance of building materials should be considered inherently in the design of future smart/green buildings. Hence, it is of vital importance to build an evaluation scheme to identify the relationship between the wireless friendliness of a building material and its EM and physical properties [34].

In this paper, we study the impact of building materials, especially their relative permittivity and thickness, on the performance of indoor line-of-sight (LOS) MIMO communications. To the best of our knowledge, this is the first attempt to study the indoor capacity from the perspective of wall material design. The main contributions of this paper are summarized as follows:

- Taking the wall reflection (WR) path into account and based on distance-dependant Rician fading model, a new indoor LOS MIMO channel model is proposed.
- The marginal probability distribution function (MPDF) of an unordered squared singular value, the ergodic capacity of the indoor LOS MIMO channel, and the squared singular values of its deterministic part are analytically obtained in closed forms. These analytical expressions reveal the relationship between the indoor MIMO channel capacity and the relative permittivity and thickness of the building material.
- We propose a scheme based on spatially averaged indoor capacity, which can be used to evaluate the wireless friendliness of building materials and to guide the design of a wireless-friendly building.
- The wireless friendliness performance of building materials is analysed. The optimal values of the permittivity and thickness of building materials that maximise the spatially averaged indoor capacity are obtained for both the omnidirectional and directional BS antenna arrays.
- The analytical results are verified through Monte Carlo simulations.

The remainder of this paper is organized as follows. Section II introduces system model for indoor LOS MIMO downlink transmissions. In Section III, the analytical MPDF of an unordered squared singular value, the ergodic capacity of an indoor LOS MIMO channel, and the squared singular values of its deterministic part are derived in closed forms. Then a scheme used for evaluating the wireless friendliness of a building material is proposed in Section IV. The impact of directional radiation pattern is discussed in Section V. Monte Carlo simulation results are provided to verify all analytical results in Section VI. Finally, Section VII concludes this paper.

II. System Model

In this section, we introduce a novel system model for indoor LOS MIMO communications that incorporates the WR path and the EM and physical properties of the building material.

We consider indoor LOS MIMO downlink transmissions, as shown in Fig. 1. In the considered room, one BS is deployed close to one of the walls and one user equipment (UE) could be arbitrarily positioned. Since the strength of a WR path from a wall other than the wall that is closest to the BS will be dominated by the distance-dependent path loss, the reflected paths from the other walls would be much weaker than the WR path from the wall closest to the BS. Hence, the considered wall refers to the wall closest to the BS hereafter, and the WR path refers to the wall reflected path from the considered wall. The BS is deployed in parallel with the considered wall with a small distance of D_1 from the wall. The BS and a typical UE are equipped with N_{T} and N_{R} omnidirectional antennas, respectively, both in linear arrays with inter-antenna spacing D. The complex frequency-flat linear channel from the BS to the typical UE is constructed as

$$\mathbf{y} = \mathbf{H}\mathbf{x} + \mathbf{n}, \tag{1}$$

where $\mathbf{x} \in \mathbb{C}^{N_{\mathrm{T}} \times 1}$, $\mathbf{y} \in \mathbb{C}^{N_{\mathrm{R}} \times 1}$ denote the transmitted signal and the received signal, respectively, $\mathbf{n}$ denotes the additive white Gaussian noise, and $\mathbf{H}$ is a $N_{\mathrm{R}} \times N_{\mathrm{T}}$ channel matrix,

$$[\mathbf{H}_{\mathrm{LOS}}]_{n_{\mathrm{R}},n_{\mathrm{T}}} = \frac{\mu}{4\pi d_1} \exp\left(-j2\pi\frac{d_1}{\mu} - j2\pi\frac{D}{\mu}\left(\left(n_{\mathrm{R}} - \frac{N_{\mathrm{R}}-1}{2}\right)\cos\left(\theta_{\mathrm{R}_1} + \Delta\theta\right) + \left(n_{\mathrm{T}} - \frac{N_{\mathrm{T}}-1}{2}\right)\cos\theta_{\mathrm{T}_1}\right)\right) \tag{2}$$

$$[\mathbf{H}_{\mathrm{WR}}]_{n_{\mathrm{R}},n_{\mathrm{T}}} = \frac{\mu\Gamma}{4\pi d_2} \exp\left(-j2\pi\frac{d_2}{\mu} - j2\pi\frac{D}{\mu}\left(\left(n_{\mathrm{R}} - \frac{N_{\mathrm{R}}-1}{2}\right)\cos\left(\theta_{\mathrm{R}_2} + \Delta\theta\right) + \left(n_{\mathrm{T}} - \frac{N_{\mathrm{T}}-1}{2}\right)\cos\theta_{\mathrm{T}_2}\right)\right) \tag{3}$$

subject to $\mathbb{E}[\mathrm{Tr}\{\mathbf{H}\mathbf{H}^{\dagger}\}] = N_{\mathrm{R}}N_{\mathrm{T}}$, where $\mathbb{E}(\cdot)$ and $\mathrm{Tr}\{\cdot\}$ denote the expectation and the trace of a matrix, respectively.

Other than the LOS path, the WR path is taken into account to capture the impact of building materials on the indoor wireless propagation channel. For a certain position in the room, the LOS path and the WR path are deterministically modelled by Friis' formula as $N_{\mathrm{R}} \times N_{\mathrm{T}}$ matrix $\mathbf{H}_{\mathrm{LOS}}$ and $\mathbf{H}_{\mathrm{WR}}$, respectively, whose elements are given in (2) and (3) on the previous page, respectively, in which $n_{\mathrm{T}} \in \{0, 1, ..., N_{\mathrm{T}} - 1\}$ and $n_{\mathrm{R}} \in \{0, 1, ..., N_{\mathrm{R}} - 1\}$ are the indices of transmit and receive antenna elements, μ denotes the wavelength of EM waves in the air, d_1 and d_2 denote the length of the LOS path and the WR path, respectively, θ_{T_1} and θ_{T_2} denote the approximated angle of departure (AoD) of the LOS path and the WR path at the BS array, respectively, while θ_{R_1} and θ_{R_2} denote the approximated angle of arrival (AoA) of the LOS path and the WR path at the UE array, respectively, $\Delta\theta$ denotes the arbitrary orientation angle of the UE array, where $\theta_{\mathrm{T}_1}, \theta_{\mathrm{T}_2}, \theta_{\mathrm{R}_1}, \theta_{\mathrm{R}_2}, \Delta\theta \in \{0, \pi\}$, $(\theta_{\mathrm{R}_1} + \Delta\theta)$ and $(\theta_{\mathrm{R}_2} + \Delta\theta)$ denote equivalent AoA of the LOS path and the WR path at the UE array, respectively, and Γ represents the equivalent reflection coefficient of the WR path.

Along the WR path, multiple internal reflections are considered when the EM wave interacts with the building material. Using plane wave far-field approximation, the incident angles of different order reflections are all approximated by α. When the building material is assumed to be a homogenous dielectric reflector with relative permittivity ε and thickness ζ, the equivalent reflection coefficient of the WR path is represented as [20]

$$\Gamma = \frac{1 - \exp(-j2\delta)}{1 - \Gamma'^{2}\exp(-j2\delta)}\Gamma', \tag{4}$$

where

$$\delta = \frac{2\pi\zeta}{\mu}\sqrt{\varepsilon - \sin^2\alpha}, \tag{5}$$

and the first-order reflection coefficient Γ' represents the transverse electric (TE) polarisation Γ_{TE} or the transverse magnetic (TM) polarisation Γ_{TM} of the incident electric field, respectively, which are given by:

$$\Gamma_{\mathrm{TE}} = \frac{\cos\alpha - \sqrt{\varepsilon - \sin^2\alpha}}{\cos\alpha + \sqrt{\varepsilon - \sin^2\alpha}}, \tag{6}$$

or

$$\Gamma_{\mathrm{TM}} = \frac{\cos\alpha - \sqrt{(\varepsilon - \sin^2\alpha)/\varepsilon^2}}{\cos\alpha + \sqrt{(\varepsilon - \sin^2\alpha)/\varepsilon^2}}. \tag{7}$$

For simplicity, $\mathbf{H}_{\mathrm{LOS}}$ and $\mathbf{H}_{\mathrm{WR}}$ are merged as one matrix $\mathbf{H_1}$, which can be decomposed as

$$\mathbf{H_1} = A_1\mathbf{h}^{\mathrm{H}}_{\beta_1}\mathbf{h}_{\alpha_1} + A_2\mathbf{h}^{\mathrm{H}}_{\beta_2}\mathbf{h}_{\alpha_2}, \tag{8}$$

$$A_1 = \frac{\mu\sqrt{N_{\mathrm{T}}N_{\mathrm{R}}}}{4\pi d_1}e^{-j2\pi\frac{d_1}{\mu}},$$

$$A_2 = \frac{\mu\Gamma\sqrt{N_{\mathrm{T}}N_{\mathrm{R}}}}{4\pi d_2}e^{-j2\pi\frac{d_2}{\mu}},$$

$$\alpha_l = 2\pi D\cos\theta_{\mathrm{T}_l}/\mu,$$

$$\beta_l = 2\pi D\cos\left(\theta_{\mathrm{R}_l} + \Delta\theta\right)/\mu,$$

$$\mathbf{h}_{\alpha_l} = \left(\frac{e^{-j\left(-\frac{N_{\mathrm{T}}-1}{2}\right)\alpha_l}}{\sqrt{N_{\mathrm{T}}}}, \frac{e^{-j\left(1-\frac{N_{\mathrm{T}}-1}{2}\right)\alpha_l}}{\sqrt{N_{\mathrm{T}}}}, ..., \frac{e^{-j\left(\frac{N_{\mathrm{T}}-1}{2}\right)\alpha_l}}{\sqrt{N_{\mathrm{T}}}}\right),$$

$$\mathbf{h}_{\beta_l} = \left(\frac{e^{j\left(-\frac{N_{\mathrm{R}}-1}{2}\right)\beta_l}}{\sqrt{N_{\mathrm{R}}}}, \frac{e^{j\left(1-\frac{N_{\mathrm{R}}-1}{2}\right)\beta_l}}{\sqrt{N_{\mathrm{R}}}}, ..., \frac{e^{j\left(\frac{N_{\mathrm{R}}-1}{2}\right)\beta_l}}{\sqrt{N_{\mathrm{R}}}}\right),$$

where $l \in \{1, 2\}$.

Based on distance-dependant Rician fading model and the multipath (MP) effect, our channel matrix $\mathbf{H}$ consists of three components including the LOS part, the WR part, and the MP part, which can be presented as

$$\mathbf{H} = \sqrt{\frac{\bar{K}}{1+\bar{K}}}\bar{\mathbf{H}} + \sqrt{\frac{1}{1+\bar{K}}}\mathbf{H}_{\mathrm{MP}}, \tag{9}$$

where the deterministic matrix $\bar{\mathbf{H}}$, including the LOS part and the WR part, is expressed as

$$\bar{\mathbf{H}} = \frac{\mathbf{H_1}}{\|\mathbf{H_1}\|}\sqrt{N_{\mathrm{R}}N_{\mathrm{T}}}, \tag{10}$$

subject to $\mathbb{E}[\mathrm{Tr}\{\mathbf{H}\mathbf{H}^{\dagger}\}] = N_{\mathrm{R}}N_{\mathrm{T}}$, with $\|\cdot\|$ denoting the F-norm. The MP components are assumed to be independent and identically distributed zero mean and unit variance complex Gaussian random variables arranged in the $N_{\mathrm{R}} \times N_{\mathrm{T}}$ matrix $\mathbf{H}_{\mathrm{MP}}$. $\bar{K}$ is the power ratio between the deterministic part $\bar{\mathbf{H}}$ and the random part $\mathbf{H}_{\mathrm{MP}}$, which can be obtained through

$$\bar{K} = KS, \tag{11}$$

where K is the distance-dependant Rician factor as a function of d_1 defining the power ratio between the LOS part and the MP part, given by [35, Eq. (5.22)]

$$K = 8.7 + 0.051d_1(\mathrm{dB}), \tag{12}$$

and

$$S = \frac{\|\mathbf{H_1}\|^2}{\|A_1\|^2} = \left|\frac{d_1^2}{d_2^2}\Gamma^2 + \frac{2Md_1}{N_{\mathrm{T}}N_{\mathrm{R}}d_2}\Gamma + 1\right|, \tag{13}$$

$$\Delta\beta = \left\langle \mathbf{h}^{\mathrm{H}}_{\beta_2}, \mathbf{h}^{\mathrm{H}}_{\beta_1} \right\rangle = \frac{1}{N_{\mathrm{R}}}\sum_{q=-(N_{\mathrm{R}}-1)/2}^{(N_{\mathrm{R}}-1)/2}\exp\left(jq(\beta_1-\beta_2)\right) = \frac{\sin\left(\pi N_{\mathrm{R}}D\left(\cos\left(\theta_{\mathrm{R}_1}+\Delta\theta\right)-\cos\left(\theta_{\mathrm{R}_2}+\Delta\theta\right)\right)/\mu\right)}{N_{\mathrm{R}}\sin\left(\pi D\left(\cos\left(\theta_{\mathrm{R}_1}+\Delta\theta\right)-\cos\left(\theta_{\mathrm{R}_2}+\Delta\theta\right)\right)/\mu\right)} \tag{16}$$

$$\Delta\alpha = \langle \mathbf{h}_{\alpha_2}, \mathbf{h}_{\alpha_1} \rangle = \frac{1}{N_{\mathrm{T}}}\sum_{q=-(N_{\mathrm{T}}-1)/2}^{(N_{\mathrm{T}}-1)/2}\exp\left(jq(\alpha_1-\alpha_2)\right) = \frac{\sin\left(\pi N_{\mathrm{T}}D(\cos\theta_{\mathrm{T}_1}-\cos\theta_{\mathrm{T}_2})/\mu\right)}{N_{\mathrm{T}}\sin\left(\pi D(\cos\theta_{\mathrm{T}_1}-\cos\theta_{\mathrm{T}_2})/\mu\right)} \tag{17}$$

in which $M = \sum_{p=0}^{N_{\mathrm{T}}-1} \sum_{q=0}^{N_{\mathrm{R}}-1} \cos\left(p\left(\alpha_1-\alpha_2\right)+q\left(\beta_1-\beta_2\right)\right)$.

III. Analysis of Ergodic Capacity

In this section, for an arbitrary position in the room, we derive the two non-zero squared singular values of $\mathbf{H_1}$, the MPDF of an unordered squared singular value and the ergodic capacity of an indoor LOS MIMO channel $\mathbf{H}$ in closed forms.

A. The distribution of the squared singular value of channel

For notational convenience, we define $m = \min\{N_{\mathrm{R}}, N_{\mathrm{T}}\}$ and $n = \max\{N_{\mathrm{R}}, N_{\mathrm{T}}\}$.

Lemma 1: Suppose $\varphi_1, \varphi_2, ..., \varphi_m$ are the m squared singular values of $\mathbf{H_1}$, where $\varphi_1, \varphi_2, ..., \varphi_{m-2} = 0$ and $\varphi_{m-1}, \varphi_m > 0$. The two non-zero squared singular values of $\mathbf{H_1}$ are computed in closed-form as

$$\varphi_{m-1} = \frac{\|\mathbf{X}\|^2 - \sqrt{\|\mathbf{X}\|^4 - 4|\det(\mathbf{X})|^2}}{2}, \tag{14}$$

$$\varphi_m = \frac{\|\mathbf{X}\|^2 + \sqrt{\|\mathbf{X}\|^4 - 4|\det(\mathbf{X})|^2}}{2}, \tag{15}$$

$$\mathbf{X} = \begin{bmatrix} A_1 + A_2\Delta\beta\Delta\alpha & A_2\Delta\beta\,\|\mathbf{h}_{\alpha_*}\| \\ A_2\Delta\alpha\,\|\mathbf{h}_{\beta_*}\| & A_2\,\|\mathbf{h}_{\alpha_*}\|\,\|\mathbf{h}_{\beta_*}\| \end{bmatrix},$$

$$\mathbf{h}^{\mathrm{H}}_{\beta_*} = \mathbf{h}^{\mathrm{H}}_{\beta_2} - \Delta\beta\mathbf{h}^{\mathrm{H}}_{\beta_1},$$
$$\mathbf{h}_{\alpha_*} = \mathbf{h}_{\alpha_2} - \Delta\alpha\mathbf{h}_{\alpha_1},$$

and $\Delta\beta$ and $\Delta\alpha$ are given in (16) and (17), respectively [36].

Proof: See Appendix. ∎

Theorem 1: The MPDF of an unordered squared singular value λ of $\mathbf{H}$ is computed in (18) [37], where the two non-zero squared singular values of $\sqrt{\bar{K}}\bar{\mathbf{H}}$ are given by

$$\phi_{m-1} = \frac{\bar{K}N_{\mathrm{R}}N_{\mathrm{T}}\varphi_{m-1}}{\|\mathbf{H_1}\|^2} = \frac{KN_{\mathrm{R}}N_{\mathrm{T}}\varphi_{m-1}}{\|A_1\|^2}, \tag{19}$$

and

$$\phi_m = \frac{\bar{K}N_{\mathrm{R}}N_{\mathrm{T}}\varphi_m}{\|\mathbf{H_1}\|^2} = \frac{KN_{\mathrm{R}}N_{\mathrm{T}}\varphi_m}{\|A_1\|^2}, \tag{20}$$

and $D_{i,j}$ is the (i,j)-co-factor of the $m \times m$ matrix $\mathbf{Z}$ whose (l,k)th entry is given by

$$(\mathbf{Z})_{l,k} = \begin{cases} (n-m+k+l-2)!, & 1 \le l \le m-2, \\ \frac{{}_1F_1(n-m+l, n-m+1, \phi_k)}{((n-m+l-1)!)^{-1}}, & \text{otherwise}. \end{cases} \tag{21}$$

The hypergeometric function ${}_0F_1\left(w, z^2\right)$ in (18) is defined in the series form by

$${}_0F_1\left(w, z^2\right) = \sum_{s=0}^{\infty} \frac{(z)^{2s}}{s![w]_s}, \tag{22}$$

and the hypergeometric function ${}_1F_1\left(e, o, g\right)$ in (21) is given by

$${}_1F_1\left(e, o, g\right) = \sum_{s=0}^{\infty} \frac{[e]_s g^s}{[o]_s s!}, \tag{23}$$

where $[r]_t = \frac{(r+t-1)!}{(r-1)!}$.

Proof: Given the channel model in (8)-(13), the channel matrix $\mathbf{H}$ is an N_{R}-by-N_{T} non-central Wishart matrix with mean $\sqrt{\frac{\bar{K}}{1+\bar{K}}}\bar{\mathbf{H}}$. Hence, the MPDF of an arbitrary squared value of $\mathbf{H}$ can be found in [37, (3)], which is derived by the squared singular values of $\sqrt{\bar{K}}\bar{\mathbf{H}}$.

Since $\mathbf{H_1}$ has only two non-zero squared singular values given in Lemma 1 and the relationship between $\mathbf{H_1}$ and $\bar{\mathbf{H}}$ is given in (10), the two non-zero squared singular values of $\sqrt{\bar{K}}\bar{\mathbf{H}}$ are given in (19) and (20), respectively, based on (14) and (15).

Meanwhile, using [37, Lemma 2], we get

$$\lim_{\tau \to \mathbf{0}} \frac{{}_0F_1\left(n-m+1, \left(\bar{K}+1\right)(\phi_i+\tau_i)\lambda\right) C_{i,j}(\phi_i+\tau_i)}{\prod_{k<l}^{m} ((\phi_l+\tau_l)-(\phi_k+\tau_k))} = \frac{f_i(\lambda) D_{i,j}(\phi_i+\tau_i)}{\prod_{l=1}^{m-2}(l-1)! \prod_{l=m-1}^{m} \phi_l^{m-2}(\phi_m-\phi_{m-1})}, \tag{24}$$

where $\tau = \{\tau_1, \tau_2, ..., \tau_m\}$ is an m-dimensional vector whose elements are distinct,

$$f_i(\lambda) = \begin{cases} \lambda^{i-1}[n-m+1]^{-1}_{i-1}, & 1 \le i \le m-2, \\ {}_0F_1\left(n-m+1, \left(\bar{K}+1\right)\phi_i\lambda\right), & \text{otherwise}, \end{cases} \tag{25}$$

$D_{i,j}$ is given in (21) and $C_{i,j}$ in [37, (3)] is the (i,j)-co-factor of the $m \times m$ matrix $\mathbf{A}$ whose (i,j)th entry is $\mathbf{A}_{i,j} = (n-m+j-1)!{}_0F_1\left(n-m+j, n-m+1, \phi_i\right)$. Since the $\mathbf{H}$ has only two non-zero squared values, its MPDF can be derived as (18) by substituting (24) and (25) into [37, (3)]. ∎

B. Closed-form ergodic capacity

Theorem 2: The ergodic capacity at a typical position is given by (26), where the average signal-to-noise-ratio (SNR)

$$f(\lambda) = \frac{e^{-\phi_m-\phi_{m-1}-(\bar{K}+1)\lambda}}{m((n-m)!)^2\lambda} \sum_{j=1}^{m} \frac{\left((\bar{K}+1)\lambda\right)^{n-m+j}}{(\phi_m\phi_{m-1})^{m-2}(\phi_m-\phi_{m-1}) \prod_{l=0}^{m-3} l!\,(n-m+l)!} \cdot \left(\sum_{i=1}^{m-2} D_{i,j}\left(\left(\bar{K}+1\right)\lambda\right)^{i-1} + \frac{{}_0F_1\left(n-m+1, (\bar{K}+1)\phi_{m-1}\lambda\right)}{(D_{m-1,j})^{-1}} + \frac{{}_0F_1\left(n-m+1, (\bar{K}+1)\phi_m\lambda\right)}{(D_{m,j})^{-1}} \right) \tag{18}$$

$$C(\rho) = \kappa \sum_{j=1}^{m} \left(\sum_{i=1}^{m-2} \frac{(\vartheta-1)!}{(D_{i,j})^{-1}} \sum_{k=1}^{\vartheta} E_{\vartheta-k+1}\left(\frac{\bar{K}+1}{\rho/N_{\mathrm{T}}}\right) + \sum_{p=0}^{\infty} \frac{\left(D_{m-1,j}\phi_{m-1}^p + D_{m,j}\phi_m^p\right)}{p!\,(n-m+p)!((\tau-1)!\,(n-m)!)^{-1}} \sum_{k=1}^{\tau} E_{\tau-k+1}\left(\frac{\bar{K}+1}{\rho/N_{\mathrm{T}}}\right) \right) \tag{26}$$

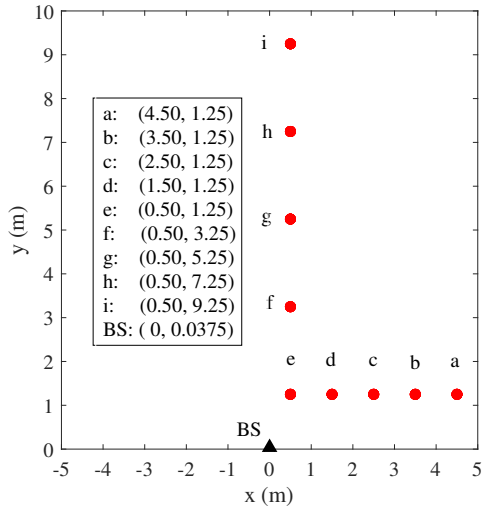

Fig. 2. Cartesian coordinates for a room, e.g. $W = L = 10$ (m), where the BS is close to the considered wall and there is an L-shaped route inside.

at each receiver branch is given by

$$\rho = \frac{\bar{K}\|\mathbf{H}_1\|^2 \rho_{\mathrm{T}}}{\left(\bar{K}+1\right) N_{\mathrm{R}} N_{\mathrm{T}}}, \tag{27}$$

in which $\rho_{\mathrm{T}} = \mathbb{E}\left(\|\mathbf{x}\|^2\right) \Big/ \mathbb{E}\left(\|\mathbf{n}\|^2\right)$ refers to the SNR at transmitter side,

$$\kappa = \frac{\exp\left(\frac{\bar{K}+1}{\mathrm{SNR}/N_{\mathrm{T}}} - \phi_m - \phi_{m-1}\right)}{\ln 2 \left((n-m)!\right)^{m-1} \left(\phi_m \phi_{m-1}\right)^{m-2} \left(\phi_m - \phi_{m-1}\right) \prod_{l=0}^{m-3} l!}, \tag{28}$$

$\vartheta = n - m + j + i - 1$, $\tau = n - m + j + p$, and $E_Q(x) = \int_1^\infty e^{-xt} t^{-Q}\, \mathrm{d}t$.

Proof: The ergodic capacity can be derived by taking the expectation with respect to λ as follows [38]

$$\begin{aligned} C(\rho) &= m\mathbb{E}\left[\log_2\left(1 + \frac{\rho}{N_{\mathrm{T}}}\lambda\right)\right] \\ &= m\int_0^\infty \log_2\left(1 + \frac{\rho}{N_{\mathrm{T}}}\lambda\right) f(\lambda)\mathrm{d}\lambda, \end{aligned} \tag{29}$$

where $f(\lambda)$ is given in (18). The integral over λ in (29) is computed by the series expansion of ${}_0F_1\left(n-m+1, \left(\bar{K}+1\right)\phi_i\lambda\right)$ in (22) and

$$\int_0^\infty \ln(1+\varpi\lambda)\lambda^{\eta-1} e^{-\gamma\lambda}\mathrm{d}\lambda = \frac{(\eta-1)!}{e^{-\frac{\gamma}{\varpi}}\gamma^\eta} \sum_{l=1}^{\eta} E_{\eta-l+1}\left(\frac{\gamma}{\varpi}\right) \tag{30}$$

in [39, Appendix A]. Thus, the ergodic capacity at a typical UE position is given in (26). ■

IV. Wireless Friendliness Evaluation Scheme for Building Materials

In this section, we investigate how friendly a wall is to indoor LOS MIMO transmissions. Aiming to quantify the wireless friendliness of a building material, a reasonable indicator is the expectation of capacity $\mathbb{E}(C)$. However, the value of $\mathbb{E}(C)$ cannot be calculated straightforwardly. An alternative solution is to average the capacity values over dense sample points inside the room, since the limit of the mean capacity values over sample points equals $\mathbb{E}(C)$ as the sampling density approaches infinity.

Algorithm 1: An Wireless Friendliness Evaluation Scheme for a Building Material

Input: ε_0, ζ, K, μ, W, L, X, Y, N_{T}, N_{R}, D, D_1, ρ_{T}
Output: C_{avg}

```
Calculate the step in x axis: Δ_x = W/X;
Calculate the step in y axis: Δ_y = (L−D_1)/(Y−1);
Determine the coordinates (x, y) of all sample points :
    x = −W/2 + (Δ_x/2) : Δ_x : W/2 − (Δ_x/2);
    y = D_1 : Δ_y : L;
Determine the BS position located at (0, D_1);
for i = 1; i ≤ X do
    for j = 1; j ≤ Y do
        Determine the UE location (x_i, y_j);
        Calculate d_1, d_2, θ_{T_1}, θ_{T_2}, θ_{R_1} and θ_{R_2}, α;
        Calculate Γ with (4)-(7);
        Constructe H with (8)-(13);
        Derive C(x_i, y_j) with (26)-(28);
Calculate C_avg with (31);
return C_avg;
```

Building a two-dimensional Cartesian coordinate system inside a $W \times L$ rectangular room as shown in Fig. 2, we take $X \times Y$ sample points spatially evenly distributed throughout the room. For a UE at the location (x_i, y_j) where $i \in \{1, 2, ..., X\}$ and $j \in \{1, 2, ..., Y\}$, its downlink ergodic capacity can be computed by (26)-(28) and denoted as $C(x_i, y_j)$ in bit/s/Hz. The capacity spatially averaged over all sample points, used as an evaluation indicator for measuring the wireless friendliness of a building material, is given by

$$C_{\mathrm{avg}} = \frac{1}{XY}\sum_{i=1}^{X}\sum_{j=1}^{Y} C(x_i, y_j). \tag{31}$$

According to [20], a simple expression of relative permittivity ε is given by $\varepsilon = \varepsilon_0 - j\varepsilon_1$, where the real part and the imaginary part can be expressed as a function of frequency f, i.e., $\varepsilon_0 = uf^v$ and $\varepsilon_1 = 17.98\sigma/f$, where $\sigma = rf^t$ is the conductivity of the building material, and constants u, v, r and t are compiled in [20, Table III]. In the following, we focus on the permittivity and thickness of the building material.

Permittivity: The permittivity in this paper refers to the real part of relative permittivity ε_0. The imaginary part is assumed to be a constant. Note that both ε and ε_0 are unitless.

Thickness: Since the building material in this paper is assumed to be a homogenous dielectric reflector, the building material's thickness of ζ equals to that of the wall.

The scheme for evaluating the wireless friendliness of a building material is given in Algorithm 1. The permittivity ε_0 and the thickness ζ of a wall material are the inputs, and the output C_{avg} is computed following (31) as an indicator of its wireless friendliness. A higher C_{avg} indicates that a wall made

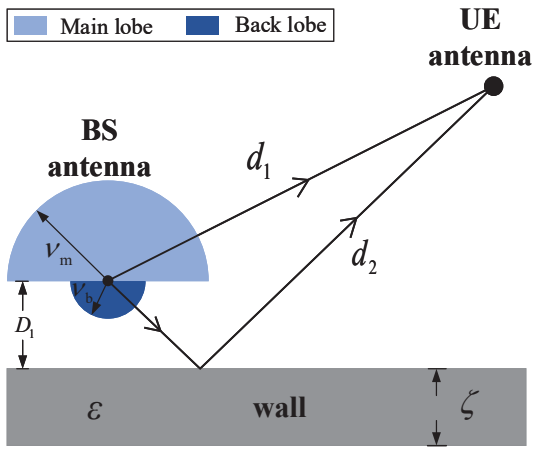

Fig. 3. The impact of the radiation pattern of a directional BS antenna on the EM propagation along the LOS path and the WR path.

of this kind of material would be more friendly to indoor LOS MIMO communications.

V. Impact of Directional Radiation Pattern

In this section, we consider each transmit element in the BS linear array as a directional antenna, as shown in Fig. 3. The main lobe directivity gain and the back lobe directivity gain are denoted as ν_{m} and ν_{b}, respectively, where $\nu_{\mathrm{m}}^2+\nu_{\mathrm{b}}^2=2$ according to the energy conservation law. Due to the dynamic attitude of UE, we assume an omnidirectional antenna for the UE antenna for analytical tractability. The deterministic part of $\mathbf{H_1}$ should be rewritten accordingly as

$$\mathbf{H}_1' = \nu_{\mathrm{m}} A_1 \mathbf{h}_{\beta_1}^{\mathrm{H}} \mathbf{h}_{\alpha_1} + \nu_{\mathrm{b}} A_2 \mathbf{h}_{\beta_2}^{\mathrm{H}} \mathbf{h}_{\alpha_2}. \tag{32}$$

The two non-zero squared singular values of $\mathbf{H}_1'$ are derived by replacing $\mathbf{X}$ in (14) and (15) with

$$\mathbf{X}' = \begin{bmatrix} \nu_{\mathrm{m}} A_1 + \nu_{\mathrm{b}} A_2 \Delta\beta\Delta\alpha & \nu_{\mathrm{b}} A_2 \Delta\beta \left\|\mathbf{h}_{\alpha_*}\right\| \\ \nu_{\mathrm{b}} A_2 \Delta\alpha \left\|\mathbf{h}_{\beta_*}\right\| & \nu_{\mathrm{b}} A_2 \left\|\mathbf{h}_{\alpha_*}\right\| \left\|\mathbf{h}_{\beta_*}\right\| \end{bmatrix}. \tag{33}$$

The $\bar{K}$ in channel model (9)-(13), the squared singular distribution of channel (18)-(20) and the ergodic capacity (26)-(28) should all be replaced by K', where $K'=KS'$, K is the Rician factor given by (12), and

$$S' = \frac{\left\|\mathbf{H}_1'\right\|^2}{\left\|A_1\right\|^2} = \left| \frac{d_1^2 \nu_{\mathrm{b}}^2}{d_2^2 \nu_{\mathrm{m}}^2} \Gamma^2 + \frac{2M d_1 \nu_{\mathrm{b}}}{N_{\mathrm{T}} N_{\mathrm{R}} d_2 \nu_{\mathrm{m}}} \Gamma + 1 \right|. \tag{34}$$

Meanwhile, the ergodic capacity $C(\rho')$ for directional antenna cases should be derived by the average SNR at each receiver antenna ρ', which is given by

$$\rho' = \frac{K' \|\mathbf{H}_1'\|^2 \rho_{\mathrm{T}}}{(K'+1) N_{\mathrm{R}} N_{\mathrm{T}}}. \tag{35}$$

The wireless friendliness evaluation scheme for directional BS antenna arrays is similar to Algorithm I by using (32)-(35).

TABLE I
Main Simulation Assumption

Parameter name	Parameter value
Frequency f (GHz)	6
Room width W (m)	10
Room length L (m)	10
Inter-antenna spacing $D=\mu/2$ (m)	0.025
The distance from BS to wall D_1 (m)	0.0375
Number of BS antennas N_{T}	4
Number of UE antennas N_{R}	4
Samples along room x axis X	100
Samples along room y axis Y	100

VI. Numerical Results

In this section, we present and analyse the numerical results for both omnidirectional and directional BS antenna arrays to present a comprehensive understanding of the impact of building materials as reflectors on indoor LOS MIMO communications. Subsection A-C show the results for the omnidirectional BS antenna array, while Subsection D shows the results for the directional BS antenna array.

The parameters used in the simulations are given in Table I. The incident wave is assumed to be TE polarised. The transmission power of the BS is assumed to be equally allocated to every transmit antenna element. The BS is deployed at point (0, D_1) and its antenna array is deployed parallel to the considered wall. In the Monte Carlo simulations, the ergodic capacity at point (x_i, y_j) is computed by

$$C_{\mathrm{sim}}(x_i, y_j) = \mathbb{E}\left[\log_2 \det\left(\mathbf{I} + \frac{\rho}{N_{\mathrm{T}}}\mathbf{H}\mathbf{H}^{\dagger}\right)\right]. \tag{36}$$

A. The ergodic capacity for a specific sample point

In this subsection, we take three points, i.e. (0.3, 0.25), (4.5, 8.0) and (-2.5, 0.55), as examples to verify the correctness of analytical expression of (18)-(20) and (26)-(28). The Rician factor K of the three points is computed by (12) accordingly. Fig. 4 depicts the MPDF of an unordered squared singular value of the LOS MIMO channel. It is found that the MPDF becomes more concentrated as K is reduced, which reveals that the squared singular values of matrix $\mathbf{H}$ are more evenly distributed and thus results in a larger ergodic capacity.

Fig. 5 shows the ergodic capacity versus the transmit SNR. The ergodic capacity increases when the transmit SNR increases. Meanwhile, a larger K leads to a lower ergodic capacity under the same transmit SNR due to the less concentrated MPDF of an unordered squared singular value of channel matrix $\mathbf{H}$.

From the results for $\Delta\theta$ being 0 and $\pi/2$ in Fig. 4 and Fig. 5, respectively, we can see that $\Delta\theta$ has a limited impact on the MPDF of an unordered squared singular value and the ergodic capacity of indoor LOS MIMO channel. This is because $\Delta\beta$ in (16) is hardly affected by $\Delta\theta$. When $\Delta\theta$ increase from 0 to π, $\Delta\beta$ is always very close to 1. As a result, the squared singular values of $\mathbf{H}$ derived by (14)-(15) will not change much with $\Delta\theta$. Consequently, the MPDF of an unordered squared singular value in (18)-(20) and the ergodic capacity in (26)-(28) of $\mathbf{H}$ will stay nearly constant for varying $\Delta\theta$.

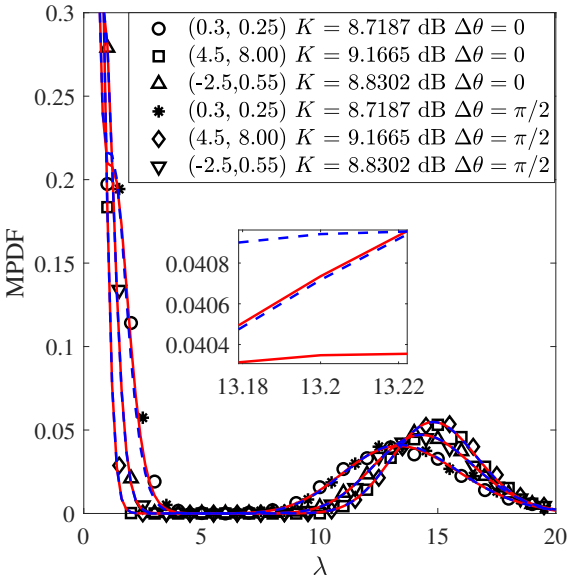

Fig. 4. The MPDF of an unordered squared singular value at three points, for $\zeta = 0.2$, $\varepsilon = 5.31 - j0.5861 f^{-0.1905}$ [20, Table III]. Markers represent simulation values while red solid lines and blue dash lines represent analytical values when $\Delta\theta = 0$ and $\Delta\theta = \pi/2$, respectively.

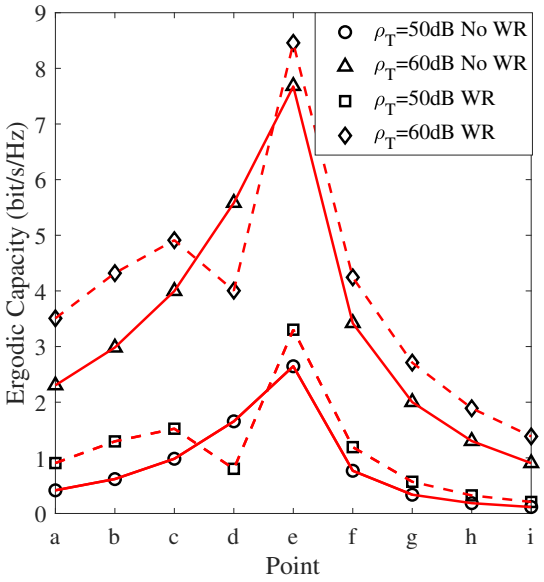

Fig. 6. Ergodic capacity at the points for L-shaped route, for $\zeta = 0.2$, $\varepsilon = 5.31 - j0.5861 f^{-0.1905}$. Markers represent simulation values while both the solid and dash lines represent analytical values.

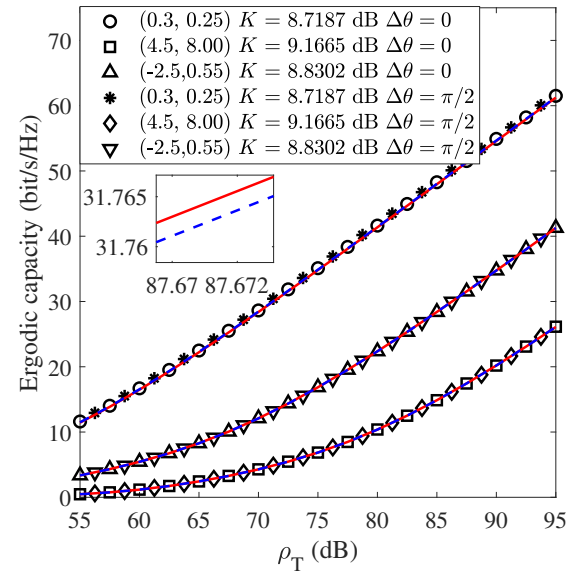

Fig. 5. Relationship between ergodic capacity and transmit SNR at three points, for $\zeta = 0.2$, $\varepsilon = 5.31 - j0.5861 f^{-0.1905}$. Markers represent simulation values while red solid lines and blue dash lines represent analytical values when $\Delta\theta = 0$ and $\Delta\theta = \pi/2$, respectively.

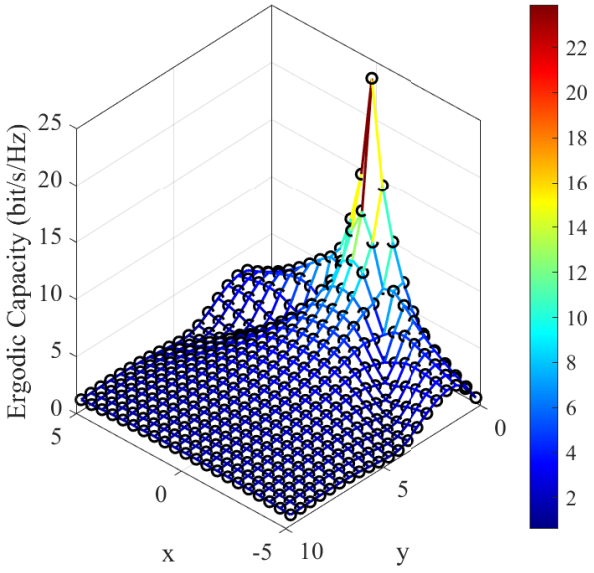

Fig. 7. Ergodic capacity distribution in the 10 m $\times$ 10 m square room, for $\rho_T = 60$ dB, $\zeta = 0.2$, $\varepsilon = 5.31 - j0.5861 f^{-0.1905}$. Markers represent simulation values while the lines represent analytical values.

Therefore, due to the space limitation, all the numerical results hereinafter are conducted when $\Delta\theta = 0$.

B. The ergodic capacity distribution in a square room

To verify the accuracy of the evaluation indicator C_{avg} in (31) and the usefulness of Algorithm 1, the ergodic capacity at different positions is studied in this subsection.

We design a L-shaped route that includes some typical UE positions in the square room, as shown in Fig. 2. The ergodic capacities from point a to j along this route, in the presence or absence of WR path, are shown in Fig. 6. The dash lines illustrate the results taking into account the WR path. From point a to e, we observe an increase in capacity as the UE is approaching the BS except for point d, where the slump in ergodic capacity is due to the power cancellation caused by

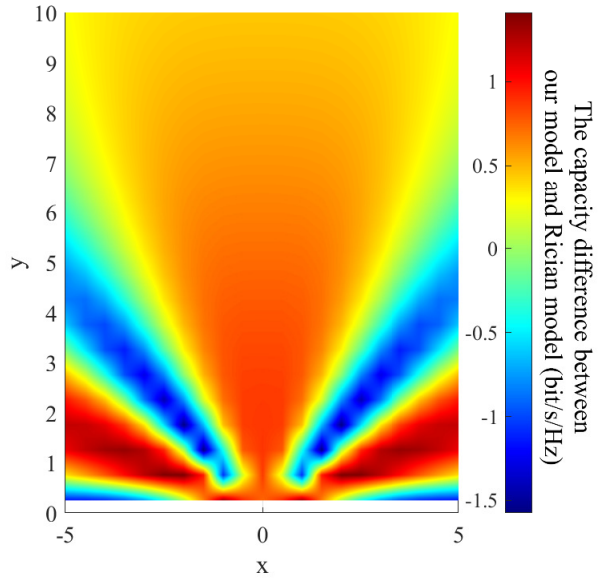

Fig. 8. The ergodic capacity difference between our proposed channel and the Rician channel, for $\rho_{\mathrm{T}} = 60$ dB, $\zeta = 0.2$, $\varepsilon = 5.31 - j0.5861 f^{-0.1905}$. The positive/negative difference indicates constructive/destructive interference.

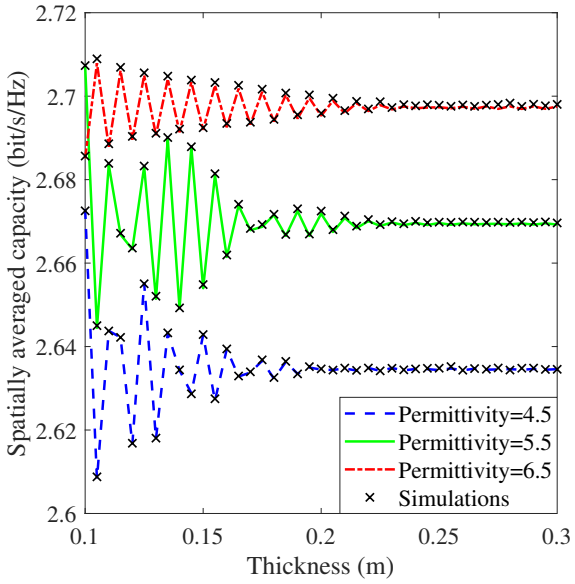

Fig. 10. Impact of wall thickness on spatially averaged capacity for the omnidirectional BS antenna array for $\rho_{\mathrm{T}} = 60$ dB.

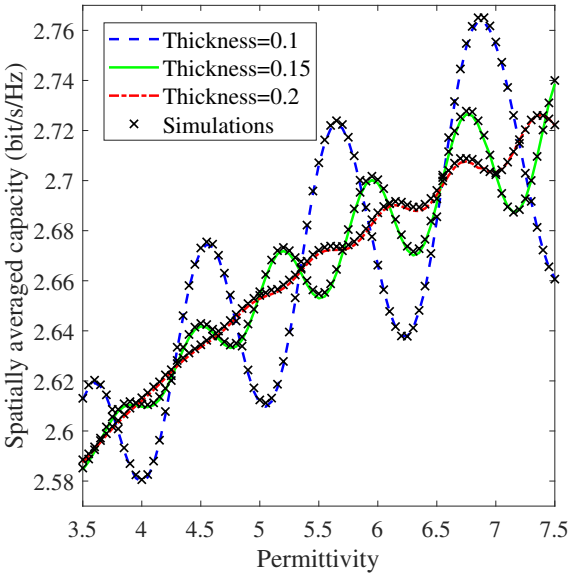

Fig. 9. Impact of wall permittivity on spatially averaged capacity for the omnidirectional BS antenna array for $\rho_{\mathrm{T}} = 60$ dB.

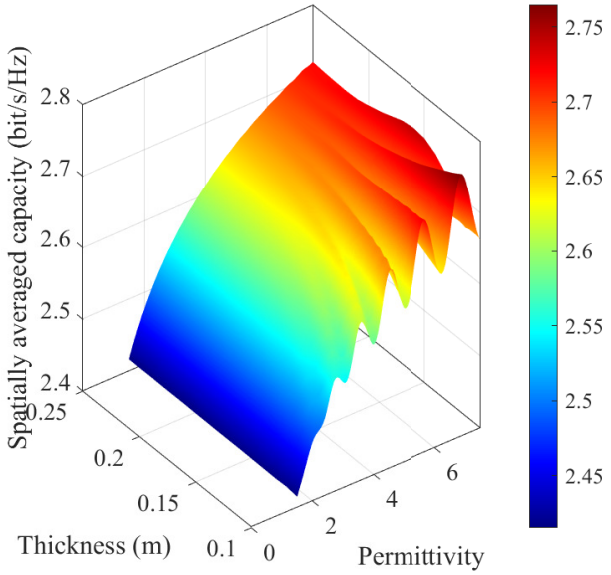

Fig. 11. The composite impact of permittivity and thickness on spatially averaged capacity for the omnidirectional BS antenna array for $\rho_{\mathrm{T}} = 60$ dB.

the destructive combination of the LOS path and the WR path. When the UE moves from point e to i, the capacity declines. This is different from the ergodic capacity under the Rician fading model without considering the WR path that would monotonically decrease with an increasing UE-BS distance, as shown by the solid lines in Fig. 6.

The spatial distribution of the ergodic capacity in a square room using our proposed model is shown in Fig. 7. It is observed that the ergodic capacity is not a monotonic function of the UE-BS distance. This phenomenon can be attributed to the constructive and destructive interference between the EM waves along the LOS path and the WR path. The length difference in $O(\lambda)$ leads to the great changes of the amplitude and phase of the superposed EM wave arriving at the UE.

Fig. 8 plots the ergodic capacity difference between our proposed channel model based on (8)-(13) and the Rician fading channel model. The position with a positive/negative difference corresponds to a location that experiences the constructive/destructive interference between the EM waves along the LOS path and the WR path. We can see that the

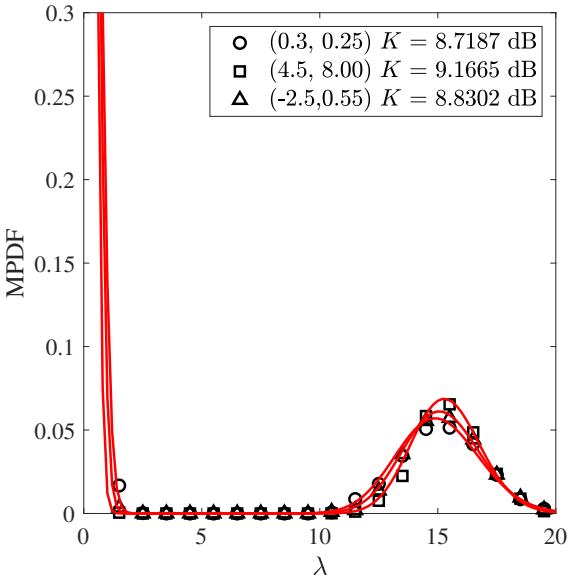

Fig. 12. The MPDF of an unordered squared singular value at three points, for $\zeta = 0.2$, $\varepsilon = 5.31 - j0.5861 f^{-0.1905}$. Markers represent simulation values while lines represent analytical values.

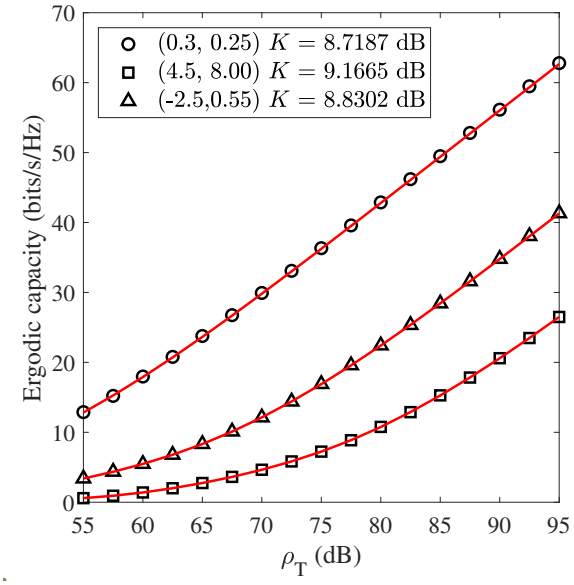

Fig. 13. Relationship between ergodic capacity and transmit SNR at three points, for $\zeta = 0.2$, $\varepsilon = 5.31 - j0.5861 f^{-0.1905}$. Markers represent simulation values while lines represent analytical values.

positions suffering from the destructive interference appear in certain directions, along which the Fabry-Pérot resonance phenomenon of EM waves is observed.

Concluded from Fig. 6-8, the impact of the WR path that characterises the EM and physical properties of building materials on indoor ergodic capacity is non-trivial, which cannot be ignored in indoor LOS MIMO communications.

C. The impact of wall permittivity and thickness on spatially averaged capacity

In order to identify a wall material with desirable wireless friendliness, the relationship between the evaluation indicator named spatially averaged capacity C_{avg} and the key parameters, i.e., the permittivity ε_0 and the thickness ζ of building materials is shown in this subsection.

Fig. 9 and Fig. 10 plot the spatially averaged capacity as a function of the permittivity and the thickness of building materials, respectively. In Fig. 9, as the permittivity increases from 3.5 to 7.5, the envelope of each spatially averaged capacity curve presents a upward trend. The variation in the spatially averaged capacity becomes more significant with the increase of the permittivity. In Fig. 10, for a given permittivity, as the wall thickness increases, the spatially averaged capacity first fluctuates with it under a decreasing envelope and gradually converges to a constant value when the thickness goes beyond 0.25 m. We observe quite severe fluctuations of the spatially averaged capacity at relatively small wall-thickness values. That is because the reflection coefficient amplitude fluctuates more severely when the wall is thinner. It should be highlighted that a tiny lapse in the wall permittivity or the thickness would bring about changes in the spatially averaged capacity of up to 0.19 bits/s/Hz.

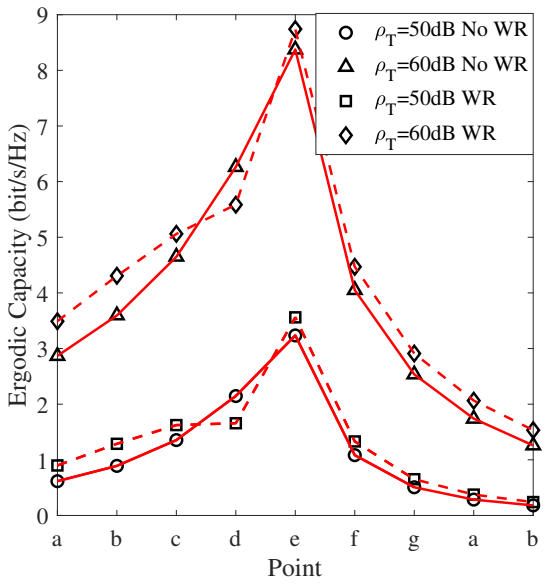

Fig. 14. Ergodic capacity at the points for L-shaped route, for $\zeta = 0.2$, $\varepsilon = 5.31 - j0.5861 f^{-0.1905}$. Markers represent simulation values while both the solid and dash lines represent analytical values.

The composite impact of the building material's permittivity and thickness on the spatially averaged capacity is illustrated in Fig. 11. When the permittivity and the thickness are configured in the range from 1.5 to 7.5 and from 0.1 to 0.25 m, respectively, we observe that the optimal parameter pair of [ε_0, ζ] resulting in the highest spatially averaged capacity of 2.763 bits/s/Hz is [6.92, 0.1], while the worst pair resulting in the lowest spatially averaged capacity of 2.415 bits/s/Hz is [1.50, 0.1]. We can conclude that certain combinations of the wall thickness and permittivity values lead

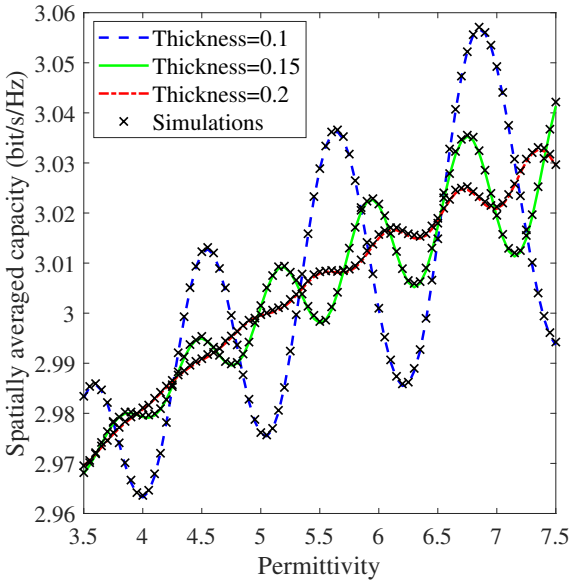

Fig. 15. Impact of wall permittivity on spatially averaged capacity for the directional BS antenna array for $\rho_{\mathrm{T}} = 60$ dB.

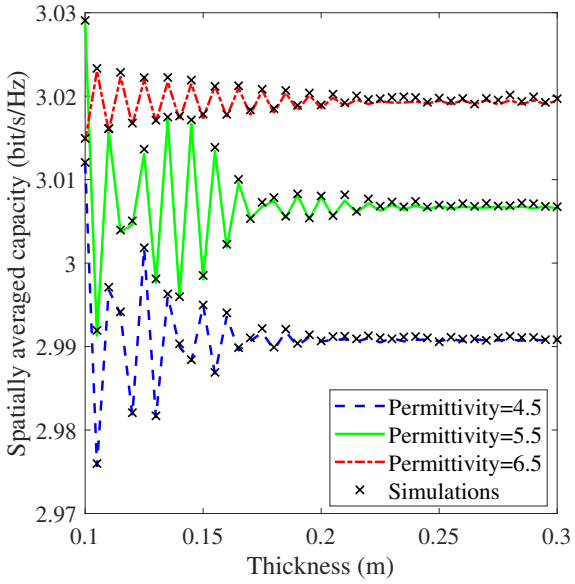

Fig. 16. Impact of wall thickness on spatially averaged capacity for the directional BS antenna array for $\rho_{\mathrm{T}} = 60$ dB.

to peak values of the spatially averaged capacity, which can be more than 14.4% higher than the lowest spatially averaged capacity values associated with some combinations of the wall thickness and permittivity values that should be avoided during the selection and/or design of building materials.

D. Analysis for directional BS antenna array

In this subsection, Fig. 12-17 depict the numerical results for the directional BS antenna array. The main lobe directivity gain and the back lobe directivity gain are assumed as $\nu_{\mathrm{m}} = \sqrt{1/3}$ and $\nu_{\mathrm{b}} = \sqrt{5/3}$, respectively.

Fig. 12 and Fig. 13 are plotted for the same three sample points shown in Fig. 4 and Fig. 5, i.e. (0.3, 0.25), (4.5, 8.0) and (-2.5, 0.55). It is found in Fig. 12 that the MPDF of an unordered squared singular value of the LOS MIMO channel becomes more concentrated and that the largest squared singular value of the LOS MIMO channel becomes larger, when compared with the omnidirectional BS antenna array in Fig. 4. Moreover, the difference between the MPDF under different Rician factor K becomes less substantial. In Fig. 13, the ergodic capacity shows an increasing trend with the rise of transmit SNR. When comparing the red lines in Fig. 5 with the red lines in Fig. 13, the ergodic capacity under the directional BS antenna array is shown to be larger than that under the omnidirectional BS antenna array.

Given the same 9 points along the L-route drawn in Fig. 2, Fig. 14 shows similar results from Fig. 6. Even though there is less change in ergodic capacity in the presence or absence of the WR path compared with the omnidirectional BS antenna array, it still appears some positions that suffer destructive interference, such as point d.

With regards to the impact of the wall permittivity and thickness on spatially averaged capacity, significant variation up to 0.093 bits/s/Hz can be observed from Fig. 15 and Fig. 16. In Fig. 17, it is found that the optimal wall parameter pair of [ε_0, ζ] leading to the highest spatially averaged capacity of 3.057 bits/s/Hz is [6.84, 0.10], while the worst pair leading to the lowest spatially averaged capacity of 2.887 bits/s/Hz is [1.50, 0.10]. The 5.9% difference in the spatially averaged capacity generated by the certain combinations of the wall permittivity and thickness is worthy to be considered.

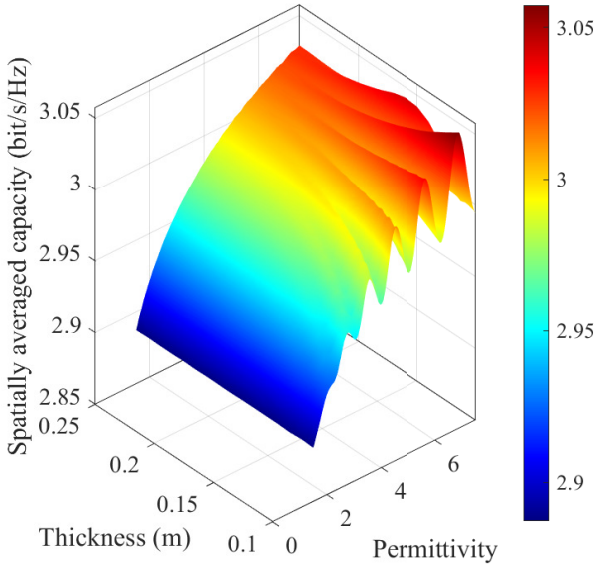

Fig. 17. The composite impact of permittivity and thickness on spatially averaged capacity for the directional BS antenna array for $\rho_{\mathrm{T}} = 60$ dB.

The results above indicate that for directional BS antenna arrays, the EM and physical properties of building materials will definitely exert a substantial influence on a room's wireless performance.

VII. Conclusions and Future works

In this paper, we firstly construct a new indoor LOS MIMO downlink channel model by considering the impact of building materials on indoor wireless performance. Then, the MPDF of the squared singular value and the ergodic capacity of the indoor LOS MIMO channel and the squared singular value of its deterministic part are obtained in closed forms. On this basis, a scheme for evaluating the wireless friendliness of building materials is provided. The analytical results are verified through Monte Carlo simulations conducted in the 6 GHz band. Numerical results demonstrate that building materials as reflectors have to be well selected or designed to avoid the risk of reducing indoor wireless performance, because a minor discrepancy in the configuration of the relative permittivity and thickness of the wall material might cause over 14.4% losses in indoor capacity.

This work is the first attempt to investigate how indoor capacity is influenced by the EM and physical properties of building materials, which has laid a solid foundation of wireless friendliness evaluation of indoor built environments. In future works, there are some extensive research directions worthy of in-depth study, including but not limit to: 1) Multi-layer building materials: It is of great necessity to analyse both single-layer and multi-layer building materials. One of the challenges is that the analytical relationship between the indoor MIMO capacity and the EM and physical properties of multi-layer building materials is hard to find due to the non-closed-form reflection coefficients [20]. Moreover, the optimal configuration of multi-layer materials would be formulated into a multi-variate optimisation problem, the complexity of which would increase with the number of layers. 2) Millimetre wave (mmWave): MmWave bands have been a promising candidate for 5G and B5G wireless network, which has been widely studied in both theoretical and experimental study. The propagation mechanism for sub-6 GHz bands and mmWave bands are substantially different due to the orders of magnitude change in the wavelength [10], [15], [40]. Hence, the work extending to mmWave bands should start from the accurate and tractable modelling of indoor mmWave propagation. Another scheme is required to evaluate the wireless friendliness of building materials at mmWave bands. 3) Experimental validation: It is critical to verify the numerical results of the proposed channel model and the evaluation scheme with experimental results. A comprehensive measurement campaign will be held in future work.

Appendix: Proof of Lemma 1

Since two deterministic components including the LOS path and the WR path are considered in our model as shown in (8), it is obvious that $\mathbf{H_1}$ has two non-zero singular values. The singular value decomposition of deterministic part $\mathbf{H_1}$ can be given as

$$\mathbf{H_1} = \mathbf{B}^{\mathrm{H}}\mathbf{X}\mathbf{A}, \tag{37}$$

where

$$\mathbf{B} = \begin{pmatrix} \mathbf{h}_{\beta_1} & \mathbf{h}_{\beta_*}/\left\|\mathbf{h}_{\beta_*}\right\| \end{pmatrix}^{\mathrm{T}},$$

$$\mathbf{A} = \begin{pmatrix} \mathbf{h}_{\alpha_1} & \mathbf{h}_{\alpha_*}/\left\|\mathbf{h}_{\alpha_*}\right\| \end{pmatrix}^{\mathrm{T}},$$

$$\mathbf{X} = \begin{pmatrix} 1 & \Delta\beta \\ 0 & \left\|\mathbf{h}_{\beta_*}\right\| \end{pmatrix} \begin{pmatrix} A_1 & 0 \\ 0 & A_2 \end{pmatrix} \begin{pmatrix} 1 & 0 \\ \Delta\alpha & \left\|\mathbf{h}_{\alpha_*}\right\| \end{pmatrix}.$$

Initially using Gram-Schmidt process, $\mathbf{h}_{\alpha_1}$ and $\mathbf{h}_{\beta_1}^{\mathrm{H}}$ are orthonormalized with $\mathbf{h}_{\alpha_*}/\|\mathbf{h}_{\alpha_*}\|$ and $\mathbf{h}_{\beta_*}^{\mathrm{H}}/\|\mathbf{h}_{\beta_*}\|$, respectively, which means that $\mathbf{B}^{\mathrm{H}}\mathbf{B}=\mathbf{I}$ and $\mathbf{A}^{\mathrm{H}}\mathbf{A}=\mathbf{I}$.

Then $\mathbf{X}$ can be simplified as a 2×2 matrix, with four elements given in (14). Assuming $\mathbf{X}$ could be decomposed as

$$\mathbf{X} = \mathbf{P}^{\mathrm{H}} \begin{pmatrix} \sqrt{\varphi_{m-1}} & 0 \\ 0 & \sqrt{\varphi_m} \end{pmatrix} \mathbf{Q}, \tag{38}$$

where $\mathbf{P}^{\mathrm{H}}\mathbf{P} = \mathbf{I}$ and $\mathbf{Q}^{\mathrm{H}}\mathbf{Q} = \mathbf{I}$, then φ_{m-1} and φ_m are two squared singular values of matrix $\mathbf{X}$. Hence we obtain

$$\mathbf{H_1} = (\mathbf{PB})^{\mathrm{H}} \begin{pmatrix} \sqrt{\varphi_{m-1}} & 0 \\ 0 & \sqrt{\varphi_m} \end{pmatrix} \mathbf{QA}. \tag{39}$$

Here it is interesting to find that φ_{m-1} and φ_m are the two squared singular values of $\mathbf{H_1}$ as well, since $(\mathbf{PB})^{\mathrm{H}}\mathbf{PB} = \mathbf{I}$ and $(\mathbf{QA})^{\mathrm{H}}\mathbf{QA} = \mathbf{I}$.

Therefore, the two non-zero squared singular values of $\mathbf{H_1}$, i.e. φ_{m-1} and φ_m, can be easily obtained by conducting singular value decomposition to low dimensional matrix $\mathbf{X}$, as given in (14) and (15), respectively.

References

[1] D. Minoli, *et al.*, "IoT considerations, requirements, and architectures for smart buildings-energy optimization and next-generation building management systems," *IEEE Internet Things J.*, vol. 4, no. 1, pp. 269-283, Feb. 2017.

[2] X. Zhang, *et al.*, "An IoT-based thermal model learning framework for smart buildings," *IEEE Internet Things J.*, vol. 7, no. 1, pp. 518-527, Jan. 2020.

[3] Y. Li, *et al.*, "Smart choice for thesmart grid: narrowband internet of things (NB-IoT)," *IEEE Internet Things J.*, vol. 5, no. 3, pp. 1505-1515, Jun. 2018.

[4] J. Santos, *et al.*, "City of things: enabling resource provisioning in smartcities," *IEEE Commun. Mag.*, vol. 56, no. 7, pp. 177-183, Jul. 2018.

[5] J. G. Andrews, *et al.*, "What will 5G be?" *IEEE J Sel. Areas Commun.*, vol. 32, no. 6, pp. 1065-1082, June, 2014.

[6] G. Gui, *et al.*, "6G: opening new horizons for integration of comfort, security and intelligence," *IEEE Wireless Commun. Mag.*, early access, 2020.

[7] Cisco, "Cisco vision: 5G-thriving indoors," Feb. 2017. [Online]. Available: cisco.com/c/dam/en/us/solutions/collateral/service-provider/ultra-services-platform/5g-ran-indoor.pdf

[8] Huawei, "Five trends to small cell 2020," *Mobile World Congress (MWC)*, Barcelona, Spain, Feb. 2016.

[9] J. Zhang, *et al.*, "Wireless energy efficiency evaluation for buildings under design based on analysis of interference gain," *IEEE Trans. Veh. Tech.*, early access, 2020.

[10] E. Bjornson, *et al.*, "Massive MIMO in sub-6 GHz and mmWave: physical, practical, and use-case differences," *IEEE Wireless Communications*, vol. 26, no. 2, pp. 100-108, April 2019.

[11] M. Jensen and J. Wallace, "A review of antennas and propagation for MIMO wireless communications," *IEEE Trans. Antennas Propag.*, vol. 52, no. 11, pp. 2810–2824, Nov. 2004.

[12] J. Zhang, *et al.*, "Bit error probability of spatial modulation over measured indoor channels," *IEEE Trans. Wirel. Commun.*, vol. 13, no. 3, pp. 1380-1387, March 2014.

[13] Y. Yang, *et al.*, "Multiband MIMO antenna for GSM, DCS, and LTE indoor applications," *IEEE Antennas Wireless Propagat. Lett.*, vol. 15, pp. 1573-1576, Jan. 2016.

[14] D. S. Shiu, *et al.*, "Fading correlation and its effect on the capacity of multielement antenna systems," *IEEE Trans. Commun.*, vol. 48, no. 3, pp. 502-513, March 2000.

[15] K. Haneda, *et al.*, "Indoor 5G 3GPP-like channel models for office and shopping mall environments," *IEEE International Conference on Communications Workshops (ICC)*, Kuala Lumpur, 2016, pp. 694-699.
[16] S. K. Yoo, *et al.*, "Ceiling- or wall-mounted access points: an experimental evaluation for indoor millimeter wave communications," *13th European Conference on Antennas and Propagation (EuCAP)*, Krakow, Poland, 2019, pp. 1-5.
[17] G. Narimani, *et al.*, "Analysis of ultrawideband pulse distortion due to lossy dielectric walls and indoor channel models," *IEEE Trans. Antennas Propag.*, vol. 64, no. 10, pp. 4423-4433, Oct. 2016.
[18] C. Jansen, *et al.*, "The impact of reflections from stratified building materials on the wave propagation in future indoor terahertz communication systems," *IEEE Trans. Antennas Propag.*, vol. 56, no. 5, pp. 1413-1419, May 2008.
[19] F. Sagnard and G. E. Zein, "In situ characterization of building materials for propagation modeling: frequency and time responses," *IEEE Trans. Antennas Propag.*, vol. 53, no. 10, pp. 3166-3173, Oct. 2005.
[20] ITU-R, "Effects of building materials and structures on radiowave propagation above about 100 MHz P series radiowave propagation," *Recomm. ITU-R P.2040-1*, Jul. 2015.
[21] L. Azpilicueta, *et al.*, "Impact of material changes in electromagnetic dosimetry estimation of complex indoor scenarios," *European Conference on Antennas and Propagation (EUCAP)*, Prague, 2012, pp. 2048-2050.
[22] V. Degli-Esposti, *et al.*, "A method for the electromagnetic characterization of construction materials based on Fabry–Pérot resonance," *IEEE Access*, vol. 5, pp. 24938-24943, Oct. 2017.
[23] H. Tian, *et al.*, "Effect level based parameterization method for diffuse scattering models at millimeter-wave frequencies," *IEEE Access*, vol. 7, pp. 93286-93293, July 2019.
[24] J. Luo, *et al.*, "Complex permittivity estimation for construction materials based on PSO method," *Proc. IEEE International Symposium on Antennas and Propagation and USNC-URSI Radio Science Meeting*, pp. 1045-1046, July 2019.
[25] J. Zhang, *et al.*, "Two-ray reflection resolution algorithm for planar material electromagnetic property measurement at the millimeter-wave bands," *Radio Science*, early access.
[26] C. Liaskos, *et al.*, "A new wireless communication paradigm through software-controlled metasurfaces," *IEEE Commun. Mag.*, vol. 56, no. 9, pp. 162–169, Sep. 2018.
[27] M. Faenzi, *et al.*, "Metasurface antennas: new models, applications and realizations," *Sci. Rep.*, vol. 9, no. 1, pp. 1–14, Jul. 2019.
[28] Q. Wu and R. Zhang, "Intelligent reflecting surface enhanced wireless network via joint active and passive beamforming," *IEEE Trans. Wirel. Commun.*, vol. 18, no. 11, pp. 5394-5409, Nov. 2019.
[29] E. Björnson and L. Sanguinetti, "Demystifying the power scaling law of intelligent reflecting surfaces and metasurfaces," Aug. 2019. [Online]. Available: https://arxiv.org/pdf/1908.03133.pdf
[30] E. Björnson, *et al.*, "Intelligent reflecting surface vs. decode-and-forward: how large surfaces are needed to beat relaying?," Jun. 2019. [Online]. Available: https://arxiv.org/pdf/1906.03949.pdf.
[31] D. Pena, *et al.*, "Measurement and modeling of propagation losses in brick and concrete walls for the 900-MHz band," *IEEE Trans. Antennas Propag.*, vol. 51, no. 1, pp. 31-39, Jan. 2003.
[32] B. Feitor, *et al.*, "Estimation of dielectric concrete properties from power measurements at 18.7 and 60 GHz," *Loughborough Antennas & Propagation Conference*, Loughborough, 2011, pp. 1-5.
[33] L. Azpilicueta, *et al.*, "Impact of material changes in electromagnetic dosimetry estimation of complex indoor scenarios," *IEEE 6th European Conference on Antennas and Propagation (EUCAP)*, Prague, 2012, pp. 2048-2050.
[34] EU H2020 AceLSAA Project. [Online]. Available: https://cordis.europa.eu/project/id/752644
[35] M. B. Zetterberg, *et al.*, "IST-2003-507581 WINNER D5.4 v1.4 final report on link level and system level channel models," Nov. 2005.
[36] E. Torkildson, *et al.*, "Indoor millimeter wave MIMO: feasibility and performance," *IEEE Trans. Wirel. Commun.*, vol. 10, no. 12, pp. 4150-4160, Dec. 2011.
[37] G. Alfano, *et al.*, "Mutual information and eigenvalue distribution of MIMO ricean channels," *Proc. IEEE Int. Symp. Inf. Theory Appl. (ISITA)*, Parma, Italy, Oct. 2004, pp. 1-6.
[38] A. Maaref and S. Aïssa, "Capacity of MIMO Rician fading channels with transmitter and receiver channel state information," *IEEE Trans. Wirel. Commun.*, vol. 7, no. 5, pp. 1687–1698, May 2008.
[39] M. Alouini and A. J. Goldsmith, "Capacity of Rayleigh fading channels under different adaptive transmission and diversity-combining techniques," *IEEE Trans. Veh. Technol.*, vol. 48, no. 4, pp. 1165-1181, Jul. 1999.
[40] I. A. Hemadeh, *et al.*, "Millimeter-wave communications: physical channel models, design considerations, antenna constructions, and link-budget," *IEEE Commun. Surveys Tuts.*, vol. 20, no. 2, pp. 870-913, Secondquarter 2018.

Yixin Zhang received the B.Eng. degree from Beijing University of Posts and Telecommunications, Beijing, China, in 2017. She is currently pursuing the Ph.D. degree in the Department of Electronic and Electrical Engineering at the University of Sheffield, Sheffield, UK. Her research interests include electromagnetic wave propagation, wireless channel modelling, MIMO antenna configurations, and indoor wireless networks.

Chen Chen received the B.Eng. degree from East China University of Science and Technology, Shanghai, China, in 2018. He is currently pursuing his Ph.D. degree in Wireless Communications at the University of Sheffield, UK. His current research interests include millimeter wave networks, green networks, stochastic geometry and machine learning.

Songjiang Yang received the B.Eng. degree with class one honours in electronic and communication engineering from the University of Sheffield, U.K., in 2017, where he is currently pursuing the Ph.D. degree. His research interests include millimetre wave channel modelling and millimetre wave wireless communications.

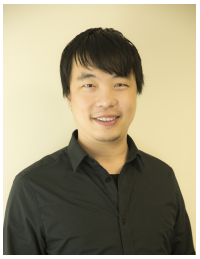

Jiliang Zhang (M'15, SM'19) received the B.E., M.E., and Ph.D. degrees from the Harbin Institute of Technology, Harbin, China, in 2007, 2009, and 2014, respectively. He was a Postdoctoral Fellow with Shenzhen Graduate School, Harbin Institute of Technology from 2014 to 2016, an Associate Professor with the School of Information Science and Engineering, Lanzhou University from 2017 to 2019, and a researcher at the Department of Electrical Engineering, Chalmers University of Technology, Gothenburg, Sweden from 2017 to 2018. He is now a Marie Curie Research Fellow at the Department of Electronic and Electrical Engineering, The University of Sheffield, Sheffield, UK. His current research interests include, but are not limited to wireless channel modelling, modulation system, relay system, wireless ranging system, vehicular communications, ultra-dense small cell networks, neural dynamic, and smart environment modelling.

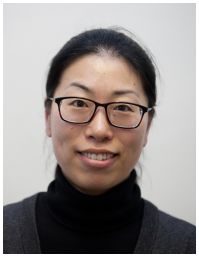

Xiaoli Chu is a Professor in the Department of Electronic and Electrical Engineering at the University of Sheffield, UK. She received the B.Eng. degree in Electronic and Information Engineering from Xi'an Jiao Tong University in 2001 and the Ph.D. degree in Electrical and Electronic Engineering from the Hong Kong University of Science and Technology in 2005. From 2005 to 2012, she was with the Centre for Telecommunications Research at Kings College London. Xiaoli has co-authored over 150 peer-reviewed journal and conference papers. She is co-recipient of the IEEE Communications Society 2017 Young Author Best Paper Award. She co-authored/co-edited the books "Fog-Enabled Intelligent IoT Systems"(Springer 2020), "Ultra Dense Networks for 5G and Beyond"(Wiley 2019), "Heterogeneous Cellular Networks: Theory, Simulation and Deployment"(Cambridge University Press 2013), and "4G Femtocells: Resource Allocation and Interference Management"(Springer 2013). She is Senior Editor for the IEEE Wireless Communications Letters, Editor for the IEEE Communications Letters, and received the IEEE Communications Letters Exemplary Editor Award in 2018. She was Co-Chair of Wireless Communications Symposium for IEEE ICC 2015, Workshop Co-Chair for IEEE GreenCom 2013, and has co-organized 8 workshops at IEEE ICC, GLOBECOM, WCNC, and PIMRC.

Jie Zhang has held the Chair in Wireless Systems at the Department of Electronic and Electrical Engineering, University of Sheffield (www.sheffield.ac.uk) since Jan. 2011.

He is also Founder, Board Chairman and Chief Scientific Officer (CSO) of Ranplan Wireless (www.ranplanwireless.com), a public company listed on Nasdaq OMX. Ranplan Wireless produces a suite of world leading indoor and the only joint indoor–outdoor 5G/4G/WiFi network planning and optimization tools suites including Ranplan Professional and Collaboration-Hub, which are being used by the world's largest mobile operators and network vendors across the globe.

Along with his students and colleagues, he has **pioneered** research in small cell and heterogeneous network (HetNet) and published some of the landmark papers and books on these topics, widely used by both academia and industry. Prof. Zhang published some of the **earliest** papers on using social media network data for proactive network optimisation. Since 2010, he and his team have developed **ground-breaking work** in modelling and designing smart built environments considering both wireless and energy efficiency. His Google scholar citations are in excess of 7000 with an H-index of 35.

Prior to his current appointments, he studied and worked at Imperial College London, Oxford University, University of Bedfordshire, and East China University of Science and Technology, reaching the rank of a Lecturer, Reader and Professor in 2002, 2005 and 2006 respectively.